

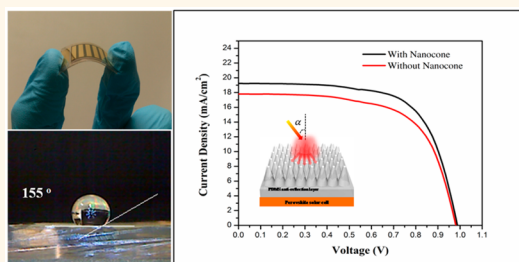
Highly Efficient Flexible Perovskite Solar Cells with Antireflection and Self-Cleaning Nanostructures

Mohammad Mahdi Tavakoli,[†] Kwong-Hoi Tsui,[†] Siu-Fung Leung,[†] Qianpeng Zhang,[†] Jin He,[‡] Yan Yao,[§] Dongdong Li,^{||} and Zhiyong Fan^{*,†}

[†]Department of Electronic and Computer Engineering, Hong Kong University of Science and Technology, Clear Water Bay, Kowloon, Hong Kong SAR, China, [‡]Shenzhen SOC Key Laboratory, PKU-HKUST Shenzhen-Hong Kong Institutions, Shenzhen 518051, China, [§]Department of Electrical and Computer Engineering, University of Houston, Houston, Texas 77204, United States, and ^{||}Shanghai Advanced Research Institute, Chinese Academy of Sciences, 99 Haik Road, Zhangjiang Hi-Tech Park, Pudong, Shanghai 201210, China

ABSTRACT Flexible thin film solar cells have attracted a great deal of attention as mobile power sources and key components for building-integrated photovoltaics, due to their light weight and flexible features in addition to compatibility with low-cost roll-to-roll fabrication processes. Among many thin film materials, organometallic perovskite materials are emerging as highly promising candidates for high efficiency thin film photovoltaics; however, the performance, scalability, and reliability of the flexible perovskite solar cells still have large room to improve. Herein, we report highly efficient, flexible perovskite

solar cells fabricated on ultrathin flexible glasses. In such a device structure, the flexible glass substrate is highly transparent and robust, with low thermal expansion coefficient, and perovskite thin film was deposited with a thermal evaporation method that showed large-scale uniformity. In addition, a nanocone array antireflection film was attached to the front side of the glass substrate in order to improve the optical transmittance and to achieve a water-repelling effect at the same time. It was found that the fabricated solar cells have reasonable bendability, with 96% of the initial value remaining after 200 bending cycles, and the power conversion efficiency was improved from 12.06 to 13.14% by using the antireflection film, which also demonstrated excellent superhydrophobicity.



KEYWORDS: perovskite solar cell · flexible glass · antireflection layer · superhydrophobicity · thermal evaporation

Organohalide perovskite materials have attracted tremendous attention in the past few years for photovoltaic applications due to a number of unique merits including simple and low-cost fabrication methods, excellent optical absorption with tunable band gaps, and long carrier diffusion lengths.^{1–5} To date, both mesoscopic and planar perovskite solar cells have achieved remarkably high efficiencies of more than 19%.^{6–10} In addition to the attractive power conversion efficiency (PCE), utilization of facile and relatively low-temperature fabrication processes to prepare perovskite layers also offers a potentially promising route to realize scalable and cost-effective photovoltaic module production.^{11–17} In order to employ perovskite solar cells for practical applications, including mobile power sources and building-integrated photovoltaics (BIPV), the

PCE needs to be optimized and the portability and flexibility should be taken into consideration in device/module design, as these properties are beneficial for the convenience of practical use and ease of installation. Typically, flexible thin film solar cells are fabricated on plastic substrates. As a matter of fact, there have been a few reports of flexible perovskite solar cells fabricated on polyethylene terephthalate (PET) and polyethylene naphthalate (PEN) plastic substrates with the highest PCE up to 12.2%.^{18–23} In addition, there are also reports on flexible perovskite solar cells on metallic foils, such as titanium, with PCE up to 10.3%.^{24,25} The perovskite solar cell fabrication process typically requires temperatures only up to 100 °C. Thermal expansion of plastic and metallic substrates for this temperature range is still significant. Thus, the thermal process may introduce stress and strain in the perovskite

* Address correspondence to eezfan@ust.hk.

Received for review July 11, 2015 and accepted August 18, 2015.

Published online 10.1021/acsnano.5b04284

© XXXX American Chemical Society

53 films as well as transparent conductive layers of
 54 devices, which result in lower PCE as compared with
 55 devices fabricated on glass substrates deposited with
 56 indium-doped tin oxide (ITO). Also, since metallic foils
 57 are not transparent, only a substrate-type device
 58 structure can be fabricated on top, whereas the
 59 optimized perovskite thin film solar cells typically have
 60 superstrate device structure. Therefore, a type of trans-
 61 parent and flexible substrate with high-temperature
 62 tolerance and low coefficient of thermal expansion
 63 (CTE) is highly desirable for high-performance
 64 applications.

65 In this work, we report the fabrication of flexible
 66 perovskite solar cells on ultrathin willow glass sub-
 67 strates using a two-step evaporation method. This type
 68 of glass is hermetic, highly transparent, dimensionally
 69 stable, impermeable to water molecules, and suitable
 70 for high-temperature processing due to its low CTE
 71 compared with that of foil and polymer substrates.²⁶
 72 The fabricated solar cell devices on the flexible glass
 73 have demonstrated PCE up to 12.06% with reasonable
 74 flexibility, retaining more than 96% of the original
 75 value after 200 mechanical bending cycles. Further-
 76 more, nanocone array films made of polydimethylsi-
 77 loxane (PDMS)^{27–31} were attached to the front surface
 78 of the devices, which demonstrated dual functions.
 79 The nanocone array produces light scattering on the
 80 front surface and thus serves as an antireflection
 81 (AR) layer, which has further improved device PCE up
 82 to 13.14%. Meanwhile, it possesses superhydrophobic

83 properties, with a water contact angle of 155°. This
 84 unique property renders the device water repellent,
 85 which not only can lead to a self-cleaning function,
 86 in general, but also is potentially beneficial for device
 87 stability since perovskite material can decompose in
 88 water quickly without proper passivation.^{6,10}

89 RESULTS AND DISCUSSION

90 In this work, perovskite thin film solar cells were
 91 fabricated on flexible willow glass (Corning) using a
 92 thermal evaporation process, as schematically shown in
 93 Figure 1a₁–a₃. The willow glass has a thickness of 50 μm,
 94 and it can withstand temperatures up to 500 °C, with a
 95 low CTE of $2.5 \times 10^{-6} \text{ K}^{-1}$. Here, we used a sub-100 °C
 96 process to fabricate perovskite thin film. Briefly, an ITO
 97 layer was sputtered on a flexible glass substrate as
 98 the transparent conductive layer, followed by sputter-
 99 ing of zinc oxide (ZnO) as an n-type compact layer.
 100 Then, a CH₃NH₃PbI₃ film was deposited on the compact
 101 layer with sequential thermal evaporation of lead iodide
 102 (PbI₂) and methylamine iodide (MAI) in a conventional
 103 thermal evaporator, followed by sample annealing
 104 at 90 °C for 45 min, in order to complete the reaction
 105 and crystallization. Afterward, 2,2',7,7'-tetrakis(*N,N*-
 106 di-*p*-methoxyphenylamine)-9,9'-spirobifluorene (Spiro-
 107 OMeTAD) was spin-coated on the perovskite film as a
 108 hole transfer layer. Finally, metal gold was thermally
 109 evaporated on Spiro-OMeTAD to complete the device
 110 as a back contact electrode. Figure 1b shows the cross-
 111 sectional SEM image of the completed device with each

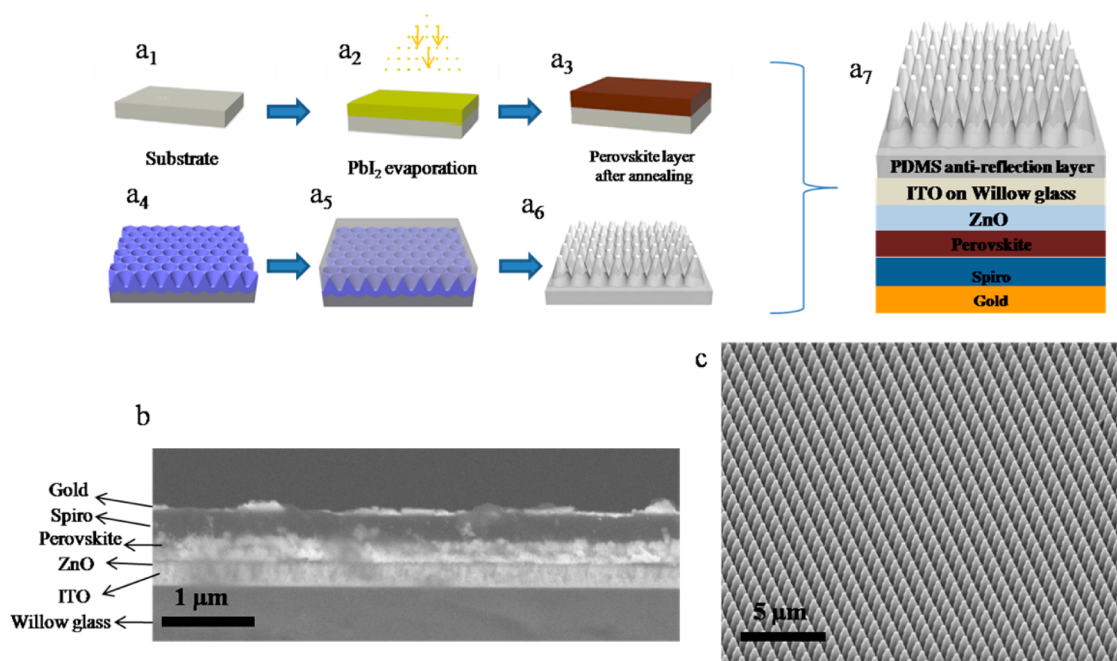


Figure 1. Schematics of perovskite solar cell and nanocone film fabrication. (a₁) Willow glass substrate. (a₂) Pbl₂ evaporation. (a₃) MAI evaporation and annealing process at 100 °C for 45 min. (a₄) Inverted cone array fabricated by a multistep anodization and wet etching process on the imprinted Al foil. (a₅) Premixed PDMS poured on a Au-coated template followed by a degassing and curing process. (a₆) Regular nanocone on flexible PDMS after peeling off. (a₇) Schematic structure of the perovskite solar cell device with nanocone PDMS film attached on the top. (b) SEM cross-sectional image of the perovskite solar cell based on a flexible glass substrate. (c) SEM image of PDMS nanocone with 1 μm pitch and 1 μm depth.

layer indicated. As the perovskite film is the key active component of the device, its properties have been characterized in detail. Figure S1a,b shows cross-sectional and top-view SEM images of the perovskite film only, suggesting that the thin film is crystalline with uniform surface coverage. Figure S1c,d displays an X-ray diffraction (XRD) pattern and photoluminescence spectrum of the perovskite thin film. The XRD pattern of $\text{CH}_3\text{NH}_3\text{PbI}_3$ perovskite indexed in Figure S1c shows that the perovskite thin film has a tetragonal crystal structure.³² Also, the photoluminescence spectrum of the perovskite film demonstrates a narrow and strong peak at 790 nm, under excitation at 405 nm laser, which indicates efficient radiative recombination. In our previous work, various nanostructures have demonstrated promising potential to improve light-harvesting capability^{33–36} and performance of solar cells.^{37–40} In this work, regular nanocone arrays were deployed on the front surface of flexible glass substrates to improve the light-capturing capability of the devices and to achieve water-repellent and self-cleaning functions at the same time. Figure 1a₄–a₆ shows the fabrication process of PDMS nanocone arrays, and Figure 1a₇ shows the final device configuration. Here, the inverted

cone (i-cone) structure achieved by multiple steps of aluminum anodization and etching was employed as a template to fabricate a nanocone PDMS AR film.³³ The tilted angle-view and top-view SEM images of the i-cone template are shown in Figure S2. Note that the evaporation method is capable of depositing uniform perovskite film in a large area, and the nanocone array fabrication is also scalable; a 4 in. willow glass wafer could be deposited with perovskite film, and AR film with the same size has been fabricated, as shown in Figure S3. However, as we have used the spin-coating process to deposit Spiro, our practical devices typically have an area of 0.04 cm².

To investigate the impact of nanocone shape on its AR property, we have fabricated PDMS nanocones with three different aspect ratios (defined by height of nanocones over periodicity) of 0.25, 0.5, and 1.0, using different i-cone templates. Figure 1c illustrates the angular view of the nanocone film with an aspect ratio of 1.0. After the AR films on the solar cell devices were deployed, optical reflectance and absorption measurements were performed and are shown in Figure 2a. It can be seen that the absorption and reflection spectra of perovskite devices with and without AR film using

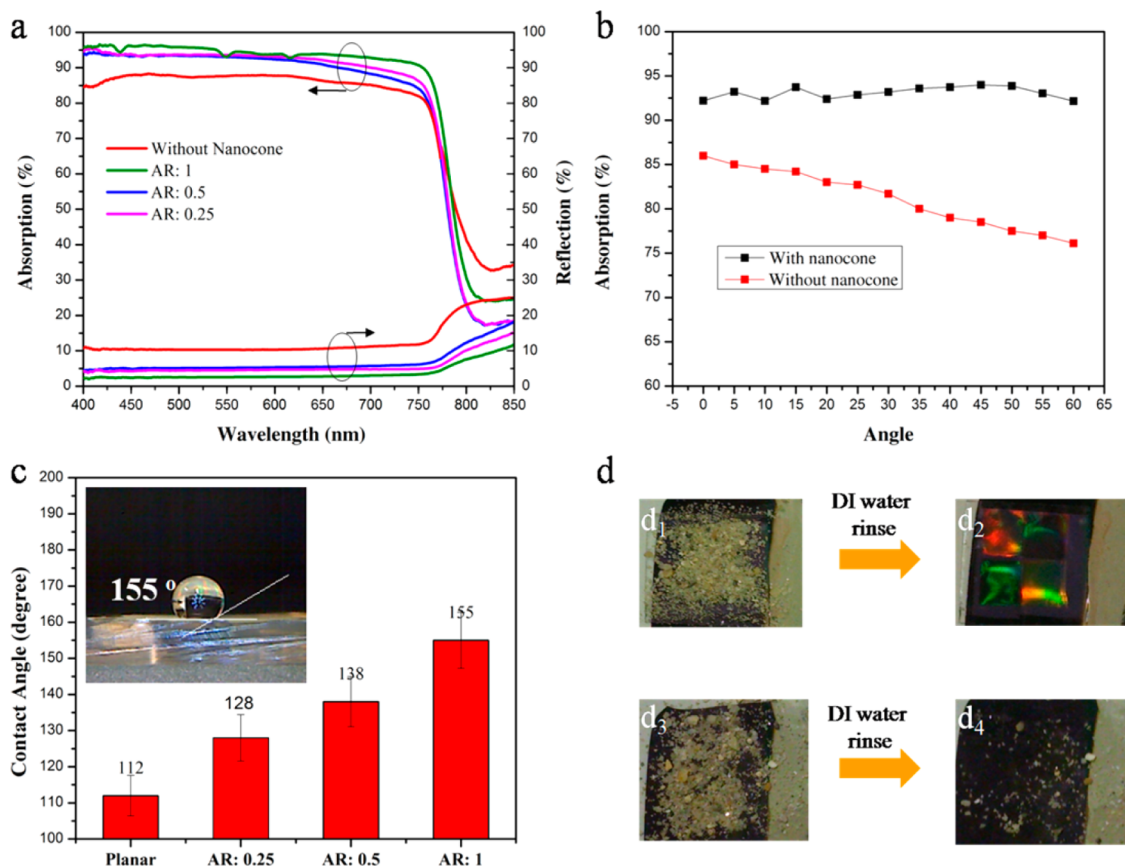


Figure 2. (a) Optical measurements of perovskite solar cell device with and without PDMS nanocone film. (b) Angular absorption of perovskite solar cell with and without PDMS nanocone film. (c) Static contact angles of deionized water on the PDMS layer with different aspect ratios. Inset image is a drop of water on the surface of the nanocone PDMS layer, with AR 1.0 showing a large contact angle of 155°. Self-cleaning experiment of the perovskite solar cell devices with (d₁, d₂) and without (d₃, d₄) a PDMS nanocone layer.

160 different aspect ratios were acquired in a wavelength
161 range from 400 to 850 nm. A homemade measurement
162 setup equipped with an integrating sphere was used
163 for measurement, and in order to calculate the absorp-
164 tion spectra, the reflectance and transmission were
165 subtracted from unity. Apparently, the reflectance of
166 the devices with the AR films was significantly reduced
167 as compared with the device without AR film in a broad
168 wavelength range. Particularly, the reflectance reduc-
169 tion is 6% for nanocone aspect ratios of 0.25 and 0.5,
170 and it is close to 8% for nanocones with an aspect ratio
171 of 1.0. The reflectance reduction is a natural result
172 of the tapered shape of nanocones, which changes
173 the effective refractive index from the air to the PDMS
174 gradually.³⁰ The higher aspect ratio nanocones on one
175 hand provide a smoother gradient of effective refrac-
176 tive index; on the other hand, a high aspect ratio
177 structure increases light scattering, which further sup-
178 presses front side reflectance. Meanwhile, the reflec-
179 tance at the willow glass/PDMS interface is negligible
180 because of the marginal difference in the refractive
181 index for PDMS and the underneath willow glass. As
182 such, it is important to avoid air bubble trapping at the
183 interface between the AR film and the glass substrate.
184 Otherwise, the reflectance will be adversely increased
185 because of an abrupt change of refractive index.
186 In addition, the absorption of solar cell devices with
187 AR layers also demonstrated 6–8% improvement, as
188 shown in Figure 2a, which is consistent with reflec-
189 tance measurement results, and the absorption spec-
190 tra also reveal that perovskite solar cells have an optical
191 band gap of ~ 1.55 eV, corresponding to a ~ 795 nm
192 optical wavelength. It is clear that, among all the AR
193 films, 1.0 aspect ratio nanocones show the lowest
194 reflection and highest absorption. Therefore, AR films
195 with 1.0 aspect ratio were utilized here for further
196 studies.

197 It is worth noting that over the time the angle of solar
198 irradiation varies during a day, therefore, omnidirec-
199 tional light-harvesting capability is important for a
200 solar panel. In this work, optical absorption of per-
201 ovskite solar cell devices with and without AR films
202 was measured for different angles of the light inci-
203 dence varying from 0° (normal incidence) to 60° in 10°
204 intervals using a focused halogen light source and an
205 integrating sphere, as shown in Figure 2b. Interest-
206 ingly, the absorption of the device with AR film remains
207 almost unchanged from 0 to 60° ; however, for the
208 device without AR film, the absorption decreases by
209 $\sim 12\%$ after increasing the incident angle to 60° . These
210 results indicate that the nanocone-based AR film helps
211 the device capture light with both a broad wavelength
212 range and a broad incident angle range.

213 It is known that organometallic perovskite materials
214 decompose quickly in water.⁶ Therefore, a water proof
215 passivation/protection packaging layer for the device
216 is crucial from a practical standpoint. In our superstrate

device structure, willow glass on the front side is dense
and water impermeable; in addition, the nanocone AR
films also have a unique water-repellent and super-
hydrophobic property. This interesting property can
avoid water accumulation on solar panels and reduce
potential risk of damaging the perovskite layer. Also,
PDMS has a strong van der Waals interaction with glass,
and as a result, PDMS can be easily attached to the
willow glass.³⁰ The static contact angles of deionized
(DI) water on the nanocone PDMS layer with different
nanocone aspect ratios are shown in Figure 2c. In order
to measure the contact angles, $2 \mu\text{L}$ of DI water
was used. It is interesting to see that a planar PDMS
substrate is hydrophobic, with a water contact angle
of 112° , and the contact angle increases monotonically
with nanocone aspect ratio with AR 1.0 nanocones
showing a contact angle up to 155° , which satisfies the
critical condition of superhydrophobicity (Figure 2c).
The reason that the contact angle increases with
aspect ratio rests in the fact that a higher aspect ratio
structure traps more air inside and typically provides
less contact area to the water droplet on the top
of nanocones.⁴¹ Besides water contact angle, roll-off
angle is also an important parameter. In reality, there
is always dust accumulation on the surface of a solar
panel, which hurts panel performance dramatically.
When the panel surface has nanostructures, the dust
will be floating on the nanostructures, and if the water
roll-off angle is small, the dust can be easily carried
away by the water droplets upon rain fall. This will lead
to a self-cleaning effect. Figure S4 shows the water roll-
off angle on different AR films. It can be seen that the
roll-off angle decreases monotonically with an increase
of nanocone aspect ratio. Aspect ratio 1.0 nanocones
can achieve a 13° roll-off angle. This small roll-off angle
indicates that the AR film may have a dust self-cleaning
function. To verify this, dust self-cleaning experiments
were carried out and are shown in Figure 2d₁–d₄.
In this process, the dust/sand particles can be easily
moved by rolling a water droplet across the surface
and removed from the device. In order to maintain the
solar panel performance for long term, a self-cleaning
property is highly desirable.

To verify the experimental results, finite-difference
time domain (FDTD) simulations were carried out
on the devices with and without AR layers. As shown
in Figure 3a, the simulated absorption spectra show a
consistent trend with the experimental ones for differ-
ent aspect ratios of AR films. As can be seen, the AR film
has a clear effect on improving the overall absorption.
In order to identify the optimal aspect ratio of PDMS
AR films, the absorption spectra of the devices with
different aspect ratios were integrated with an AM1.5G
solar spectrum (Figure 3b). The results illustrate
that AR films improve the integrated absorption by
around $1 \text{ mA}/\text{cm}^2$, and the 1.0 aspect ratio shows the
best absorption, which has a good agreement with

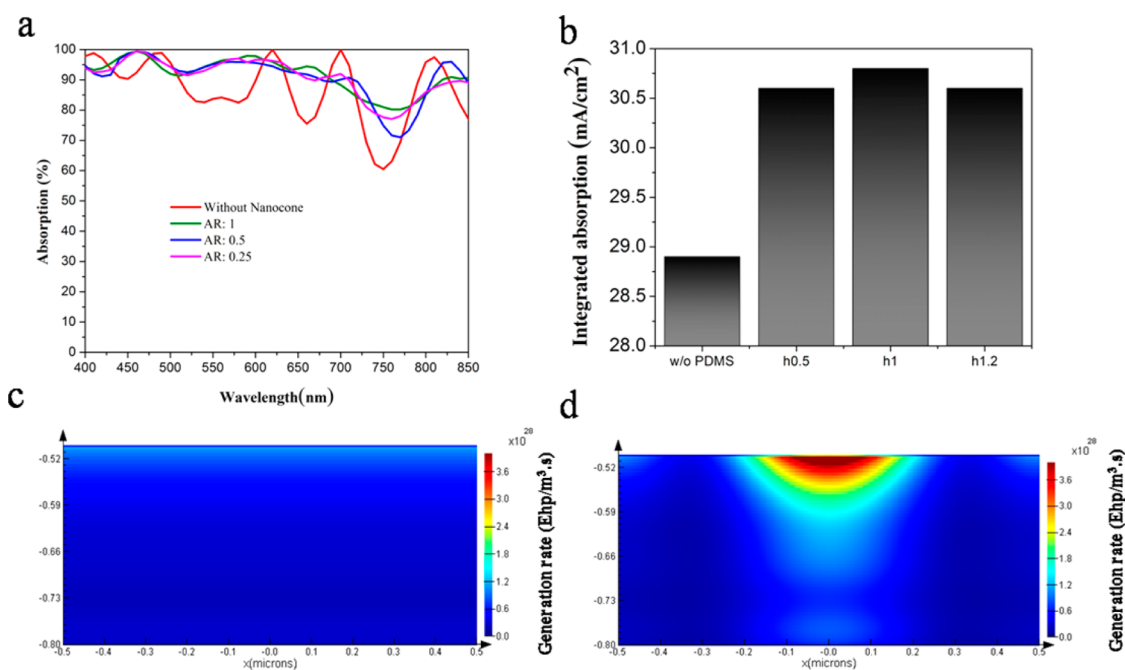


Figure 3. FDTD simulation. (a) Absorption spectra and (b) integrated absorption of perovskite thin film integrated with nanocone PDMS films with different aspect ratios. Integrated absorption is calculated by integrating absorption spectra with an AM1.5G solar spectrum. Generation rate (number of absorbed photons/ m^3/s) in the perovskite layer (c) without and (d) with PDMS nanocone film with AR 1.0. The maximum values of the color bars are both 2×10^{28} photons/ m^3/s , with red showing a high generation rate and blue showing a low generation rate.

274 experimental results. To shed more light on the detailed
 275 absorption situation inside the perovskite layer, the
 276 generation rate profiles for devices with and without
 277 AR films are shown in Figure 3c,d. When the two
 278 profiles are compared, the absorption of the device
 279 with AR film shows a clear focusing effect inside the
 280 perovskite layer, leading to significant absorption
 281 enhancement in the perovskite solar cell. Interestingly,
 282 the hot spot of generation was found right below the
 283 nanocone structure, inside the active perovskite layer,
 284 as shown in Figure S5. This clearly indicates the benefit
 285 of introducing the nanocone structure on top of the
 286 device.

F4 287 Figure 4a shows the photograph of a nanocone AR
 288 film naturally attached on the perovskite solar cell
 289 based on flexible glass. The performance of the same
 290 device with and without AR films has been characterized
 291 systematically. Figure 4b presents current density–
 292 voltage (J – V) characteristics of a representative device
 293 under 1 sun simulated illumination. The figures of merit
 294 for this device together with average performance of
T1 295 multiple devices are summarized in Table 1. The
 296 J – V curves show that the J_{sc} increases from 17.7 to
 297 19.3 mA/cm^2 after attaching the nanocone AR film
 298 on the top side of the solar cell device, which results
 299 in an enhancement in the PCE from 12.06 to 13.14%,
 300 corresponding to a $\sim 9\%$ increment. This can be clearly
 301 attributed to the enhancement of light absorption using
 302 AR film, as shown in Figure 2a. As presented in Table 1,
 303 this conclusion is consistent for 10 devices with an
 304 average PCE of 10.6 and 11.7%, without and with AR

film, respectively. This improvement can also be con-
 305 firmed with external quantum efficiency measurements,
 306 as shown in Figure 4c. As can be seen, the AR effect
 307 contributes to the entire wavelength range, which
 308 proves that the AR film is effective enough to harness
 309 visible light. In order to study the effect of scan direction,
 310 the forward and reverse scan direction were performed
 311 as shown in Figure S6. The results show that there
 312 is nearly no considerable change in the J – V curves.
 313 In addition, J_{sc} and PCE of the devices with and without
 314 AR film were measured at different incident angles,
 315 as shown in Figure 4d. Note that both J_{sc} and PCE are
 316 normalized with the horizontal light projection area on
 317 the device when it is inclined under the collimated
 318 irradiation, in order to have a fair comparison with the
 319 condition where the device is not inclined with normal
 320 light incidence. Because the AR film can be easily
 321 attached and detached, the same device was also
 322 used for the measurements. Apparently, the absolute
 323 enhancement of J_{sc} and PCE for devices with AR film
 324 is nearly 1.5–2.5 mA/cm^2 and 1–1.75%, respectively.
 325 More interestingly, with increasing light incident angle,
 326 both J_{sc} and PCE drop much faster without AR film,
 327 as compared to the case with AR film. Particularly, the
 328 efficiency of the device with AR film for a 60° incident
 329 angle is improved by 20% compared with the reference
 330 sample. This confirms the observation from Figure 2b,
 331 where the nanocones have omnidirectional light-
 332 harvesting capability. This property is highly attractive
 333 for solar panels without a mechanical solar tracking
 334 system.
 335

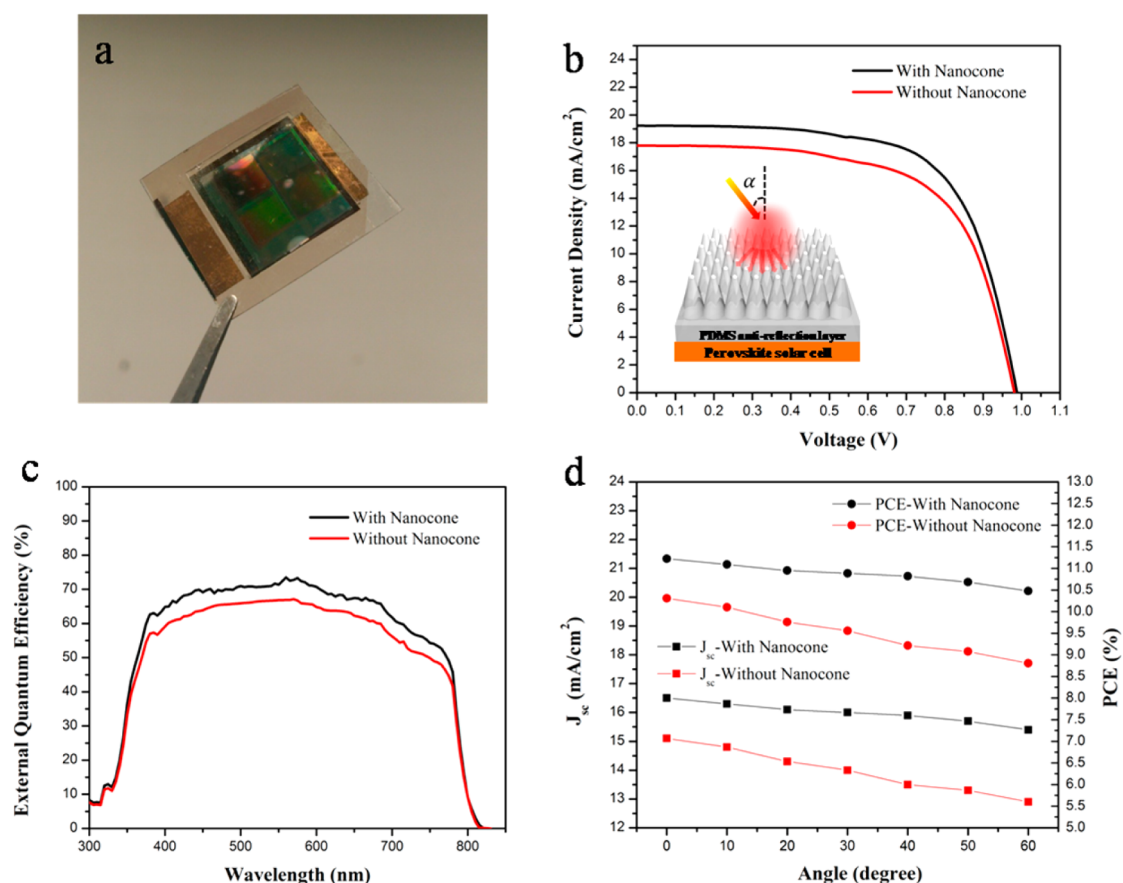


Figure 4. (a) Photograph of perovskite solar cell based on flexible willow glass integrated with a nanocone PDMS layer. (b) J - V measurements of perovskite solar cell devices with and without PDMS nanocone film (inset image is the schematic of light scattering in the device with a nanocone layer). (c) QE measurement of perovskite devices with and without a PDMS nanocone film. (d) J_{sc} and PCE of a perovskite solar cell device with and without a PDMS nanocone film obtained at different incident angles of light.

TABLE 1. Figures of Merit for the Solar Cell Devices with and without AR Films

devices	V_{oc} (V)	J_{sc} (mA/cm^2)	fill factor (%)	efficiency (%)	average of PCE (%)
without nanocone	0.97	17.7	70	12.06	10.6
with nanocone	0.98	19.3	69	13.14	11.7

device was found to be 90° , beyond that, the flexible glass substrate is prone to break. The effect of the bending cycles on the photovoltaic parameters of the device is presented in Figure 5b. The results show that J_{sc} , open-circuit voltage (V_{oc}), and fill factor (FF) were only marginally reduced through the bending tests. Specifically, J_{sc} , V_{oc} , and FF of the flexible device were reduced from 18.3 to 18.11 mA/cm^2 , from 0.98 to 0.97 V, and from 0.65 to 0.64, respectively. As a result, the PCE of the device is decreased from 11.7 to 11.24% after 200 bending cycles. As shown in Figure S8, during bending cycles, microcracks and delamination could be produced at the interfaces between different layers of the perovskite solar cells, which would deteriorate the device and increase the series resistance of devices. It is noteworthy that in the current device structure there is no backside passivation, and the entire device is not packaged; thus the active layer is not in the mechanical neutral plane during bending. With proper packaging and placement of the films in the mechanical neutral plane, the bending side effects can be minimized and performance degradation upon bending is expected to be much less.

Flexibility is a desirable feature of solar cells for many applications, such as mobile power sources and BIPV. In this work, 50 μm thickness renders willow glass and our perovskite solar cells with respectable flexibility. Figure 5a shows a photograph of a flexible device. The variation of PCE versus bending angle for a willow-glass-based perovskite solar cell is shown in Figure S7. Note that the change of light projection area on the device during a bending process is considered when calculating the power conversion efficiency. To examine the bendability of the devices, we used a solar cell with a length of 3 cm and bent it to a radius of 4 cm by applying mechanical force up to 200 cycles, then after each cycle, the device performance was measured repetitively. The maximum bending angle of a flexible

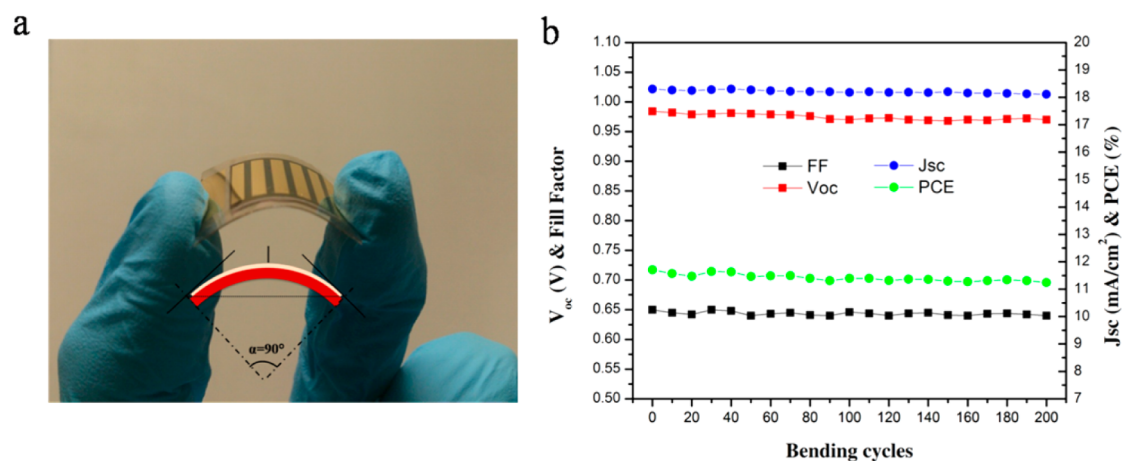


Figure 5. (a) Photograph of perovskite solar-cell-based flexible willow glass. (b) Efficiency stability depending on bending cycle in perovskite solar cells based on a willow glass substrate.

375 CONCLUSIONS

376 In summary, we demonstrated flexible $\text{CH}_3\text{NH}_3\text{PbI}_3$
 377 perovskite solar cells fabricated on ultrathin willow
 378 glasses using an evaporation method. A willow glass
 379 substrate is transparent, waterproof, and compatible
 380 with high-temperature processes with a low thermal
 381 expansion coefficient. These attractive properties
 382 make flexible glass a suitable replacement for flexible
 383 polymer substrates. On this type of flexible substrate,
 384 we have achieved device performance up to 12.06%.
 385 Meanwhile, the device performance was further
 386 improved to 13.14% by adding a layer of nanocone
 387 AR film on the front surface of willow glass to
 388 enhance light absorption. In addition, the AR film also

demonstrated a water-repellent feature with a water
 389 contact angle up to 155° and a roll-off angle of 13° .
 390 These properties lead to an interesting dust self-cleaning
 391 function which helps to maintain solar panel cleanliness
 392 and stable power output. In the end, the flexibility of the
 393 devices has been evaluated with 200 bending cycles.
 394 It was found that device performance was not signifi-
 395 cantly affected by repetitive bending. Overall, to our
 396 best knowledge, the device performance reported here
 397 is among the best for flexible perovskite solar cells.
 398 The processes developed here open up a promising
 399 route for large-scale and cost-effective production
 400 of high-performance thin film photovoltaics, which
 401 are not limited to organometallic perovskite materials.
 403

404 METHODS

405 **Preparation of Nanocone AR and SC Layer.** Aluminum foil
 406 (0.25 mm thick, 99.99% purity, Alfa Aesar) was polished electro-
 407 chemically and imprinted using a hexagonally ordered nano-
 408 pillar silicon stamp with a pitch of $1\ \mu\text{m}$ and a height of 200 nm
 409 in order to create nanostructured indentation on the Al foil.
 410 The i-cone pattern was fabricated on the imprinted Al foil by
 411 multistep anodization using an acidic solution and proper DC
 412 voltage, followed by a wet etching processes.^{30,33,34} Afterward,
 413 50 nm thick gold was thermally evaporated on the i-cone array
 414 as an antisticking layer. Then, the PDMS solution (Sylgard 184,
 415 Dow Corning, 10:1 ratio with the curing agent) was drop-cast
 416 on the Au-coated i-cone template followed by a degassing process
 417 and then cured at 80°C for 2 h. Finally, PDMS nanocone films
 418 with a thickness of 0.2 mm and different nanocone heights were
 419 peeled off directly from the i-cone template.

420 **Methylamine Iodide Preparation.** Methylamine (27.8 mL, 33 wt %
 421 in ethanol, Sigma-Aldrich) was added dropwise to 30 mL of
 422 hydroiodic acid (57 wt % in water, Sigma-Aldrich) in a 250 mL
 423 three-neck flask and mixed at 0°C for 2 h to complete the
 424 reaction. The MAI powder was recovered from the solution using
 425 a rotary evaporator at 50°C followed by dissolving in absolute
 426 ethanol and precipitating by adding diethyl ether to the solution.
 427 Finally, the MAI powder was dried at 60°C overnight in a vacuum
 428 oven.

429 **Device Fabrication.** The 50 μm thick willow glass pieces were
 430 purchased from Corning Company (USA) and cleaned prior
 431 to use by the following procedure. First, they were immersed
 432 in acetone (Merck) and then DI water (Milipore, $18\ \text{M}\Omega\cdot\text{cm}$)

containing 3 vol % of Triton X-100 and sonicated for 30 min for
 433 each solution. The specimens were then rinsed with DI water
 434 and sonicated in isopropyl alcohol for 30 min, rinsed with DI
 435 water again, sonicated in a DI water batch for another 30 min,
 436 and finally dried by blowing with air. Thereafter, they were
 437 coated with 300 nm thick ITO followed by 50 nm thick zinc oxide
 438 as an electron transport layer using sputtering. Then, a two-step
 439 thermal evaporation method was employed to deposit the
 440 organohalide perovskite film on the substrates. Specifically,
 441 the PbI_2 and MAI ($\text{CH}_3\text{NH}_3\text{I}$) were loaded onto two different
 442 quartz crucibles and then evaporated sequentially onto the ZnO
 443 compact-layer-coated ITO willow glass substrates under high
 444 vacuum (4×10^{-6} mbar) with a deposition rate of 0.1–0.2 nm/s.
 445 The vapor deposition rate was controlled using a quartz sensor
 446 and calibrated after measuring the thickness of PbI_2 and
 447 $\text{CH}_3\text{NH}_3\text{I}$ films. The sources were located at the bottom of the
 448 chamber with an angle of 90° with respect to the substrates.
 449 The distance between source and substrate was 20 cm. We fixed
 450 the evaporation rate in a range of 0.08–0.15 nm/s. Since the
 451 relative composition of $\text{CH}_3\text{NH}_3\text{I}$ to PbI_2 and the overall depos-
 452 ited thickness are two key parameters to improve the device
 453 performance, we optimized them for evaporation method.
 454 Finally, we found that a 1:1 ratio of $\text{CH}_3\text{NH}_3\text{I}$ to PbI_2 and a
 455 thickness of 340 nm of the perovskite film were the best
 456 conditions in order to achieve optimal device performance.
 457 The as-deposited films were annealed at 90°C for 45 min
 458 in the Ar-filled tube furnace. Thereafter, Spiro-OMeTAD (Lumtec,
 459 Taiwan) solution (80 mg/mL chlorobenzene) with 17.5 mL
 460 of Li-bis(trifluoromethanesulfonyl)imide (Li-TFSI)/acetonitrile
 461

462 (500 mg/mL) and 28.5 mL of TBP as additives was deposited on
463 the perovskite film by a spin-coating process (3000 rpm for 40 s).
464 Then the devices were left in a desiccator overnight, and finally,
465 100 nm thick gold was deposited by thermal evaporation
466 (0.08 nm/s) as an electrode. The device area was 0.04 cm².

467 **Film Characterization.** Field-emission scanning electron micro-
468 scopy (JEOL JSM-7100F) and X-ray diffraction method (Bruker
469 D8 X-ray diffractometer, USA) utilizing Cu K α radiation were used
470 to study the thickness, morphology, roughness of the films, and
471 phase characterization. The optical absorption and steady-state
472 photoluminescence spectra were recorded on a Varian Cary
473 500 spectrometer (Varian, USA) and an Edinburgh Instruments
474 FLS920P fluorescence spectrometer, respectively.

475 **Device Characterization.** The AM1.5G solar spectrum was simu-
476 lated by an Abet Class AAB Sun 2000 simulator with an intensity
477 of 100 mW cm⁻² calibrated with a KG5-filtered Si reference
478 cell. The current–voltage (*I*–*V*) data were measured using a
479 2400 series sourcemeter (Keithley, USA). *I*–*V* sweeps (forward
480 and backward) were performed between –1.2 and +1.2 V,
481 with a step size of 0.02 V and a delay time of 150 ms at
482 each point. External quantum efficiency spectra were recorded
483 versus wavelength with a constant white light bias of nearly
484 5 mW cm⁻² using an Oriel QE-PV-SI (Newport Corporation).

485 **FDTD Simulation.** The FDTD simulation was conducted with
486 the Lumerical FDTD software package. Plane waves with wave-
487 lengths ranging from 300 to 900 nm were utilized. A unit cell
488 of the PDMS nanocone hexagonal array was studied, and a
489 periodic boundary condition was utilized.⁴² Power absorption
490 was calculated with eq 1:

$$P_{\text{abs}} = -0.5\omega|E|^2\text{imag}(\epsilon) \quad (1)$$

491 where P_{abs} is the absorbed power per unit volume, ω is the
492 angular frequency, E is the electrical field, and $\text{imag}(\epsilon)$ is the
493 imaginary part of the dielectric permittivity. Only P_{abs} inside the
494 perovskite layer was considered. Furthermore, the absorption
495 spectrum can be integrated with the AM1.5G solar spectrum
496 to obtain the integrated absorption. If the internal quantum
497 efficiency is assumed to be 100%, then the integrated absorp-
498 tion will be equal to the generation rate, namely, generated
499 electron–hole pairs per unit volume per second. In order to
500 model the antireflection films on a perovskite solar cell, a 5 μm
501 thick layer of PDMS on top of FTO glass was employed.

502 **Conflict of Interest:** The authors declare no competing
503 financial interest.

504 **Acknowledgment.** This work was supported by the General
505 Research Fund (project 612113) from the Hong Kong Research
506 Grant Council, the Hong Kong Innovation and Technology Fund
507 (project ITS/117/13, ITS/362/14FP) from the Innovation and
508 Technology Commission, State Key Laboratory on Advanced
509 Displays and Optoelectronics at HKUST, Shenzhen Technology
510 Innovation Commission projects JCYJ20130402164725025
511 and JCYJ20140721163526514. Y.Y. acknowledges the financial
512 support from TcSUH.

513 **Supporting Information Available:** The Supporting Informa-
514 tion is available free of charge on the ACS Publications website
515 at DOI: 10.1021/acsnano.5b04284.

516 Characterization of perovskite materials, SEM images of
517 AAO template, photographs of large-scale flexible perov-
518 skite solar cell and antireflection film, roll-off angles of
519 DI water on the surface of the nanocone PDMS film, models
520 of FDTD simulation, and *J*–*V* measurement of the device
521 with different scan direction, variation of PCE versus bend-
522 ing angle of flexible device, and top-view SEM image of
523 perovskite solar cell after 200 bending cycles (PDF)

524 REFERENCES AND NOTES

525 1. Stranks, S. D.; Eperon, G. E.; Grancini, G.; Menelaou, C.;
526 Alcocer, M. J. P.; Leijtens, T.; Herz, L. M.; Petrozza, A.; Snaith,
527 H. J. Low-Temperature Solution-Processed Perovskite Solar
528 Cells with High Efficiency and Flexibility. *Science* **2013**, *342*,
529 341–344.

2. Nie, W.; Tsai, H.; Asadpour, R.; Blancon, J. C.; Neukirch, A. J.;
530 Gupta, G.; Crochet, J. J.; Chhowalla, M.; Tretiak, S.; Alam,
531 M. A.; et al. High-Efficiency Solution-Processed Perovskite
532 Solar Cells with Millimeter-Scale Grains. *Science* **2015**, *347*,
533 522–525.
3. Tavakoli, M. M.; Gu, L.; Gao, Y.; Reckmeier, C.; He, J.; Rogach,
534 A. L.; Yao, Y.; Fan, Z. Fabrication of Efficient Planar Perov-
535 skite Solar Cells Using a One-Step Chemical Vapor Deposi-
536 tion Method. *Sci. Rep.* **2015** in press.
4. Dong, Q.; Fang, Y.; Shao, Y.; Mulligan, P.; Qiu, J.; Cao, L.;
537 Huang, J. Electron-Hole Diffusion Lengths > 175 μm in
538 Solution-Grown CH₃NH₃PbI₃ Single Crystals. *Science* **2015**,
539 347, 967–970.
5. Kazim, S.; Nazeeruddin, M. K.; Grätzel, M.; Ahmad, S.
540 Perovskite as Light Harvester: A Game Changer in Photo-
541 voltaics. *Angew. Chem., Int. Ed.* **2014**, *53*, 2812–2824.
6. Stoumpos, C. C.; Malliakas, C. D.; Kanatzidis, M. G.
542 Semiconducting Tin and Lead Iodide Perovskites with
543 Organic Cations: Phase Transitions, High Mobilities, and
544 Near-Infrared Photoluminescent Properties. *Inorg. Chem.*
545 **2013**, *52*, 9019–9038.
7. Rong, Y.; Tang, Z.; Zhao, Y.; Zhong, X.; Venkatesan, S.;
546 Graham, H.; Patton, M.; Jing, Y.; Guloy, A. M.; Yao, Y. Solvent
547 Engineering Towards Controlled Grain Growth in Perov-
548 skite Planar Heterojunction Solar Cells. *Nanoscale* **2015**, *7*,
549 10595.
8. Lee, M. M.; Teuscher, J.; Miyasaka, T.; Murakami, T. N.;
550 Snaith, H. J. Efficient Hybrid Solar Cells Based on Meso-
551 Superstructured Organometal Halide Perovskites. *Science*
552 **2012**, *338*, 643–647.
9. Liu, M.; Johnston, M. B.; Snaith, H. J. Efficient Planar
553 Heterojunction Perovskite Solar Cells by Vapour Deposition.
554 *Nature* **2013**, *501*, 395–398.
10. National Renewable Energy Laboratory. Best Research-
555 Cell Efficiencies; [http://www.nrel.gov/ncpv/images/](http://www.nrel.gov/ncpv/images/efficiency_chart.jpg)
556 [efficiency_chart.jpg](http://www.nrel.gov/ncpv/images/efficiency_chart.jpg) (accessed March 20, 2015).
11. Tavakoli, M. M.; Aashuri, H.; Simchi, A.; Kalytchuk, S.; Fan, Z.
557 Quasi Core/Shell Lead Sulfide/Graphene Quantum Dots
558 for Bulk Heterojunction Solar Cells. *J. Phys. Chem. C* **2015**,
559 10.1021/acs.jpcc.5b04195.
12. Liu, D.; Kelly, T. L. Perovskite Solar Cells with a Planar
560 Heterojunction Structure Prepared Using Room-Temperature
561 Solution Processing Techniques. *Nat. Photonics* **2014**, *8*,
562 133–138.
13. Kojima, A.; Teshima, K.; Shirai, Y.; Miyasaka, T. Organometal
563 Halide Perovskites as Visible-Light Sensitizers for Photo-
564 voltaic Cells. *J. Am. Chem. Soc.* **2009**, *131*, 6050–6051.
14. Hodes, G. Perovskite-Based Solar Cells. *Science* **2013**, *342*,
565 317–318.
15. Tavakoli, M. M.; Simchi, A.; Aashuri, H. Supercritical Syn-
566 thesis and *In Situ* Deposition of PbS Nanocrystals with
567 Oleic Acid Passivation for Quantum Dot Solar Cells. *Mater.*
568 *Chem. Phys.* **2015**, *156*, 163–169.
16. Burschka, J.; Pellet, N.; Moon, S.; Humphry-Baker, R.; Gao, P.;
569 Nazeeruddin, M. K.; Grätzel, M. Sequential Deposition as
570 a Route to High-Performance Perovskite-Sensitized Solar
571 Cells. *Nature* **2013**, *499*, 316–319.
17. Tavakoli, M. M.; Tayyebi, A.; Simchi, A.; Aashuri, H.;
572 Outokesh, M.; Fan, Z. Physicochemical Properties of Hybrid
573 Graphene–Lead Sulfide Quantum Dots Prepared by
574 Supercritical Ethanol. *J. Nanopart. Res.* **2015**, *17*, 1–13.
18. Wang, X.; Li, Z.; Xu, W.; Kulkarni, S. A.; Batabyal, S. K.; Zhang,
575 S.; Cao, A.; Wong, L. H. TiO₂ Nanotube Arrays Based Flexible
576 Perovskite Solar Cells with Transparent Carbon Nanotube
577 Electrode. *Nano Energy* **2015**, *11*, 728–735.
19. Kumar, M. H.; Yantara, N.; Dharani, S.; Graetzel, M.;
578 Mhaisalkar, S.; Boix, P. P.; Mathews, N. Flexible, Low-
579 Temperature, Solution Processed ZnO-Based Perovskite Solid
580 State Solar Cells. *Chem. Commun.* **2013**, *49*, 11089–11091.
20. You, J.; Hong, Z.; Yang, Y. M.; Chen, Q.; Cai, M.; Song, T.;
581 Chen, C.; Lu, S.; Liu, Y.; Zhou, H. Low-Temperature Solution-
582 Processed Perovskite Solar Cells with High Efficiency and
583 Flexibility. *ACS Nano* **2014**, *8*, 1674–1680.
21. Roldán-Carmona, C.; Malinkiewicz, O.; Soriano, A.;
584 Espallargas, G. M.; García, A.; Reinecke, P.; Kroyer, T.;
585 600
586
587
588
589
590
591
592
593
594
595
596
597
598
599
600
601
602
603
604

- 605 Dar, M. I.; Nazeeruddin, M. K.; Bolink, H. J. Flexible High
606 Efficiency Perovskite Solar Cells. *Energy Environ. Sci.* **2014**,
607 *7*, 994–997.
- 608 22. Kim, B. J.; Kim, D. H.; Lee, Y.-Y.; Shin, H.-W.; Han, G. S.; Hong,
609 J. S.; Mahmood, K.; Ahn, T. K.; Joo, Y.-C.; Hong, K. S.; et al.
610 Highly Efficient and Bending Durable Perovskite Solar
611 Cells: Toward a Wearable Power Source. *Energy Environ.*
612 *Sci.* **2015**, *8*, 916–921.
- 613 23. Docampo, P.; Ball, J. M.; Darwich, M.; Eperon, G. E.; Snaith,
614 H. J. Efficient Organometal Trihalide Perovskite Planar-
615 Heterojunction Solar Cells on Flexible Polymer Substrates.
616 *Nat. Commun.* **2013**, *4*, 1–6.
- 617 24. Jung, H. S.; Park, N. G. Perovskite Solar Cells: From Materials
618 to Devices. *Small* **2015**, *11*, 10–25.
- 619 25. Troughton, J.; Bryant, D.; Wojciechowski, K.; Carnie, M. J.;
620 Snaith, H.; Worsley, D. A.; Watson, T. M. Highly Efficient,
621 Flexible, Indium-Free Perovskite Solar Cells Employing
622 Metallic Substrates. *J. Mater. Chem. A* **2015**, *3*, 9141–
623 9145.
- 624 26. Rance, W. L.; Burst, J. M.; Meysing, D. M.; Wolden, C. A.;
625 Reese, M. O.; Gessert, T. A.; Metzger, W. K.; Garner, S.; Cimo,
626 P.; Barnes, T. M. 14%-Efficient Flexible CdTe Solar Cells
627 on Ultra-Thin Glass Substrates. *Appl. Phys. Lett.* **2014**, *104*,
628 143903.
- 629 27. Raut, H. K.; Ganesh, V. A.; Nair, A. S.; Ramakrishna, S. Anti-
630 Reflective Coatings: A Critical, in Depth Review. *Energy*
631 *Environ. Sci.* **2011**, *4*, 3779–3804.
- 632 28. Leung, S. F.; Yu, M.; Lin, Q.; Kwon, K.; Ching, K. L.; Gu, L.;
633 Yu, K.; Fan, Z. Efficient Photon Capturing with Ordered
634 Three-Dimensional Nanowell Arrays. *Nano Lett.* **2012**, *12*,
635 3682–3689.
- 636 29. Guldin, S.; Kohn, P.; Stefk, M.; Song, J.; Divitini, G.; Ecarla, F.;
637 Ducati, C.; Wiesner, U.; Steiner, U. Self-Cleaning Antireflective
638 Optical Coatings. *Nano Lett.* **2013**, *13*, 5329–5335.
- 639 30. Chen, J.; Chang, W.; Huang, C.; Sun, K. Biomimetic Nano-
640 structured Antireflection Coating and Its Application on
641 Crystalline Silicon Solar Cells. *Opt. Express* **2011**, *19*, 14411–
642 14419.
- 643 31. Tsui, K. H.; Lin, Q.; Chou, H.; Zhang, Q.; Fu, H.; Qi, P.; Fan, Z.
644 Low-Cost, Flexible, and Self-Cleaning 3D Nanocone Anti-
645 Reflection Films for High-Efficiency Photovoltaics. *Adv.*
646 *Mater.* **2014**, *26*, 2805–2811.
- 647 32. Baikie, T.; Fang, Y.; Kadro, J. M.; Schreyer, M.; Wei, F.;
648 Mhaisalkar, S. G.; Graetzel, M.; White, T. J. Synthesis and
649 Crystal Chemistry of the Hybrid Perovskite (CH₃NH₃)PbI₃
650 for Solid-State Sensitised Solar Cell Applications. *J. Mater.*
651 *Chem. A* **2013**, *1*, 5628–5641.
- 652 33. Lin, Q.; Leung, S.; Lu, L.; Chen, X.; Chen, Z.; Tang, H.; Su, W.;
653 Li, D.; Fan, Z. Inverted Nanocone-Based Thin Film Photo-
654 voltaics with Omnidirectionally Enhanced Performance.
655 *ACS Nano* **2014**, *8*, 6484–6490.
- 656 34. Gao, Y.; Jin, H.; Lin, Q.; Li, X.; Tavakoli, M. M.; Leung, S.; Tang,
657 W. M.; Zhou, L.; Chan, H. L. W.; Fan, Z. Highly Flexible
658 and Transferable Supercapacitors with Ordered Three-
659 Dimensional MnO₂/Au/MnO₂ Nanospire Arrays. *J. Mater.*
660 *Chem. A* **2015**, *3*, 10199–10204.
- 661 35. Qiu, Y.; Leung, S. F.; Zhang, Q.; Hua, B.; Lin, Q.; Wei, Z.; Tsui,
662 K. H.; Zhang, Y.; Yang, S.; Fan, Z. Efficient Photoelectro-
663 chemical Water Splitting with Ultrathin Films of Hematite
664 on Three-Dimensional Nanophotonic Structures. *Nano Lett.*
665 **2014**, *14*, 2123–2129.
- 666 36. Kapadia, R.; Fan, Z.; Takei, K.; Javey, A. Nanopillar Photo-
667 voltaics: Materials, Processes, and Devices. *Nano Energy*
668 **2012**, *1*, 132–144.
- 669 37. Kapadia, R.; Fan, Z.; Javey, A. Design Constraints and
670 Guidelines for CdS/CdTe Nanopillar Based Photovoltaics.
671 *Appl. Phys. Lett.* **2010**, *96*, 103116.
- 672 38. Lin, Q.; Hua, B.; Leung, S. F.; Duan, X.; Fan, Z. Efficient Light
673 Absorption with Integrated Nanopillar/Nanowell Arrays
674 for Three-Dimensional Thin-Film Photovoltaic Applications.
675 *ACS Nano* **2013**, *7*, 2725–2732.
- 676 39. Yu, R.; Ching, K. L.; Lin, Q.; Leung, S. F.; Arcrossito, D.; Fan, Z.
677 Strong Light Absorption of Self-Organized 3-D Nanospire
678 Arrays for Photovoltaic Applications. *ACS Nano* **2011**, *5*,
679 9291–9298.
40. Leung, S. F.; Gu, L.; Zhang, Q.; Tsui, K. H.; Shieh, J. M.; Shen,
680 C. H.; Hsiao, T. H.; Hsu, C. H.; Lu, L.; Li, D.; et al. Roll-to-Roll
681 Fabrication of Large Scale and Regular Arrays of Three-
682 Dimensional Nanospikes for High Efficiency and Flexible
683 Photovoltaics. *Sci. Rep.* **2014**, *4*, 4243.
41. Choi, W.; Tuteja, A.; Mabry, J. M.; Cohen, R. E.; McKinley,
684 G. H. A Modified Cassie–Baxter Relationship to Explain
685 Contact Angle Hysteresis and Anisotropy on Non-Wetting
686 Textured Surfaces. *J. Colloid Interface Sci.* **2009**, *339*, 208–
687 216.
42. Tavakoli, M. M.; Tavakoli, R.; Davami, P.; Aashuri, H. A
688 Quantitative Approach to Study Solid State Phase
689 Coarsening in Solder Alloys Using Combined Phase-
690 Field Modeling and Experimental Observation. *J. Comput.*
691 *Electron.* **2014**, *13*, 425–431.